Localization of Au Nanoclusters on Layered Double Hydroxides Nanosheets: Confinement-Induced Emission Enhancement and Temperature-Responsive Luminescence

Rui Tian, Shitong Zhang, Mingwan Li, Yuqiong Zhou, Bo Lu, Dongpeng Yan, Min Wei,* David G. Evans, and Xue Duan*

Gold nanoclusters (Au NCs) stand for a new type of fluorescent nanomaterials with outstanding optical properties due to their discrete electronic energy and direct electron transition. However, relative low quantum yield (QY) of Au NCs in aqueous or solid state has limited their photofunctional applications. To improve the fluorescent performances of Au NCs and find an effective approach for the fabrication of Au NCs-based films, in this work, Au NCs are localized onto 2D layered double hydroxides (LDHs) nanosheets via a layer-by-layer assembly process; the as-fabricated (Au NCs/LDH)$_n$ ultrathin films (UTFs) show an ordered and dense immobilization of Au NCs. The localization and confinement effects imposed by LDH nanosheets induce significantly increased emissive Au(I) units as confirmed by X-ray photoelectron spectroscopy and periodic density functional theoretical simulation, which further results in promoted QY (from 2.69% to 14.11%) and prolonged fluorescence lifetime (from 1.84 μs to 14.67 μs). Moreover, the ordered (Au NCs/LDH)$_n$ UTFs exhibit well-defined temperature-dependent photoluminescence (PL) and electrochemiluminescence (ECL) responses. Therefore, this work supplies a facile strategy to achieve the immobilization of Au NCs and obtain Au NCs-based thin films with high luminescent properties, which have potential applications in PL and ECL temperature sensors.

1. Introduction

Nanoclusters (NCs, such as Au, Ag, Cu, and Pt) are ultrasmall nanoparticles (≈2 nm) with discrete electronic energy levels and unique molecule-like properties,[1–3] which have been widely used in sensing, molecular recognition, and biomedical studies.[4–7] Taking Au NCs as an example, several interesting features (e.g., nonblinking, good biocompatibility, water solubility as well as photostability against photobleaching) have afforded their extraordinary optical/chemical properties.[8–11] To stabilize Au NCs, thiolate and protein have usually been employed as ligands to avoid large agglomeration.[12,13] However, both the liquid and solid-state quantum yields (QYs) of the luminescent thiolate- and protein-protected Au NCs are still much lower than those well-established chromophores (such as inorganic quantum dots and organic fluorescent dyes),[14–16] which has largely restricted their application in optical imaging. From this viewpoint, great efforts have been focused on the improvement of the QY of Au NCs, and it was recognized that the Au(I)-thiol portion serves as the dominate emission resource that shows a great influence on the luminescent performance of typical Au NCs.[17–20] Therefore, the optimization of Au(I)-thiol units plays a key role in high-efficiency emissive Au NCs.

To develop Au NCs as practical optical/luminescent devices, the construction of ordered structures and/or arrays with high QY is of great importance, although most studies on Au NCs are focused on aqueous and powdered states to date. To achieve this goal, the incorporation of raw materials of NCs into solid matrix (such as transparent glass) has been proposed.[21,22] However, this method is limited by the category of NCs due to their different reduction potential (e.g., only Ag NCs are easy to be reduced); in addition, the common solid matrix cannot dedicate to the improvement of fluorescent performance of NCs. It is therefore eager to find a facile approach to fabricate ordered Au NCs solid-state structures with improved fluorescent properties by virtue of the interactions between Au NCs and solid matrix.

In this work, the immobilized Au NCs film materials with high QY were achieved based on the assembly of Au NCs and layered double hydroxides (LDHs) nanosheets (**Scheme 1**). LDHs nanosheet is a positively charged 2D graphene-like ultrathin structure that consists of edge-sharing metal-hydroxide octahedra (di- and trivalent metal cations coexist in a certain ratio), which has been used as a building block to construct various multifunctional materials.[23–27] Taking advantages of electropositive LDH nanosheets, Au NCs (protected by

R. Tian, Dr. S. Zhang, M. Li, Y. Zhou, B. Lu,
Prof. D. Yan, Prof. M. Wei,
Prof. D. G. Evans, Prof. X. Duan
State Key Laboratory of Chemical
Resource Engineering
Beijing University of Chemical Technology
Beijing 100029, P. R. China
E-mail: yandp@mail.buct.edu.cn; weimin@mail.buct.edu.cn

DOI: 10.1002/adfm.201501433

© 2015 WILEY-VCH Verlag GmbH & Co. KGaA, Weinheim

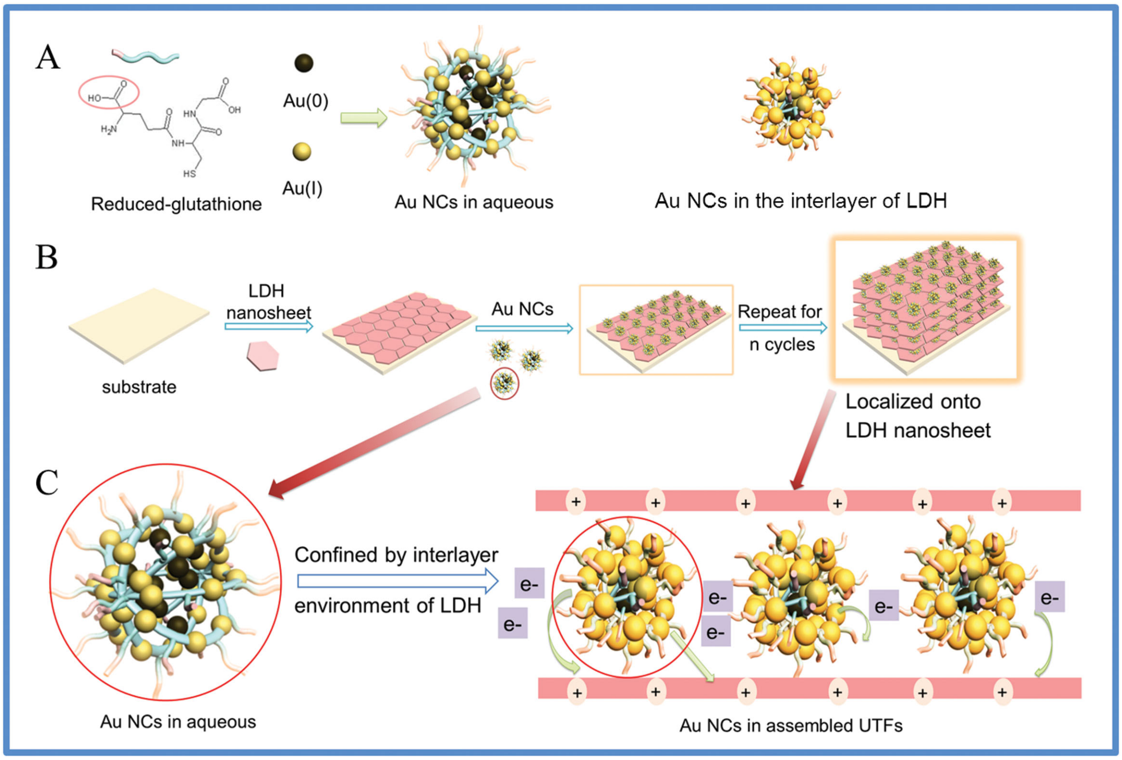

Scheme 1. Schematic representations for A) weak-emissive Au NCs in aqueous solution and strong-emissive Au NCs in UTFs, B) the LbL fabrication of multilayer luminous (Au NCs/LDH)$_n$ UTFs, and C) transformation of Au NCs from aqueous solution into interlayer microenvironment of LDHs.

negatively charged ligands) can be densely anchored onto LDH nanosheets and a periodic long-range ordered array is further constructed based on a layer-by-layer (LbL) assembly process. The positively charged LDH nanosheets can polarize the charge distribution of localized Au NCs effectively and thus increase the content of emissive Au(I)-thiol units in NCs, as confirmed by X-ray photoelectron spectroscopy (XPS) and periodic density functional theoretical (DFT) calculation. Due to the confinement and localization effects in the ordered structure, the as-fabricated ordered ultrathin films (UTFs) of (Au NCs/LDH)$_n$ exhibit improved QY (up to 14.11%) and prolonged fluorescence lifetime (14.67 µs) compared with Au NCs in aqueous solution. Moreover, these UTFs present temperature-responsive photoluminescence (PL) and electrochemiluminescence (ECL) performances, which may find applications in the fields of optical display and sensing.

2. Results and Discussion

2.1. Assembly of the (Au NCs/LDH)$_n$ UTFs

The synthesis of Au NCs is carried out through a mild reduction of HAuCl$_4$ solution by L-glutathione.[18] The obtained size of Au NCs can be estimated to be ≈1.92 and ≈2.29 nm as observed from transmission electron microscope (TEM) and atomic force microscope (AFM), respectively (Figures S1 and S2, Supporting Information), since the later involves the additional thickness of outer glutathione ligands (illustrated as SG). The characteristic absorption peak of Au NCs in the UV–vis spectra at ≈400 nm (Figure S3, Supporting Information) arises from intraband (sp←sp) or interband (sp←d) transitions,[28] and the typical absorption (≈520 nm) from the surface plasmon resonance for large-sized Au nanoparticles cannot be observed. By the use of LbL process (Scheme 1B), (Au NCs/LDH)$_n$ UTFs were obtained and monitored by UV–vis spectra. The absorption band of (Au NCs/LDH)$_n$ UTFs is observed at ≈400 nm without any shift or broadening for different cycles (**Figure** 1A), suggesting a uniform and stable microenvironment of Au NCs during the LbL process. Moreover, the band intensity at ≈400 nm enhances gradually along with the increase of deposition cycle n and a linear correlation is observed (Figure 1C), indicating a stepwise and regular film growth procedure. The loading content of Au NCs for these (Au NCs/LDH)$_n$ (n = 4–20) UTFs is determined by inductively coupled plasma atomic emission spectroscopy (ICP-AES). The Au density enhances linearly from 0.65 to 21.5 µg cm^{-2} as n increases from 4 to 20 (Figure S4 and Table S1, Supporting Information), which is visually confirmed by the gradually deepened color of these UTFs (Figure 1B). In addition, a decreased band gap of Au NCs after anchoring to the LDH nanosheets is deduced by comparing the UV–vis diffuse reflectance spectra (Figure S5, Supporting Information) with that of the aqueous solution, which is possibly related to the confinement effect of the nanogallery between the LDH layers.

© 2015 WILEY-VCH Verlag GmbH & Co. KGaA, Weinheim

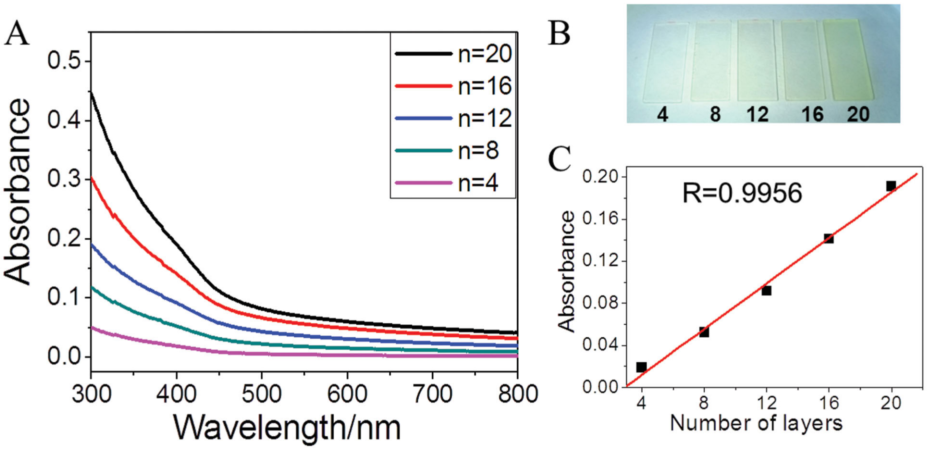

Figure 1. UV–vis monitoring of (Au NCs/LDH)$_n$ (n = 0–20) UTFs for A) UV–vis absorption spectra, B) photographs taken under daylight, and C) the increasing absorbance at 400 nm.

2.2. The Morphological and Structural Studies on the (Au NCs/LDHs)$_n$ UTFs

The morphological and structural properties of fabricated (Au NCs/LDHs)$_n$ UTFs were further studied. The lateral size of LDH nanosheets ranges in 300–500 nm (Figure S6, Supporting Information), which could serve as good candidate to localize Au NCs with the size of ≈2 nm.[29,30] For the pristine Au NCs, the average size is ≈1.92 nm as obtained from the histogram of TEM (Figure S1, Supporting Information), while their size shrinks to ≈1.58 nm within the assembled (Au NCs/LDHs)$_n$ UTFs (**Figure 2**A,B). These phenomena can be attributed to the host–guest interaction (e.g., electrostatic force and hydrogen bonding) between LDH nanosheets and Au NCs, and thus the configuration of Au NCs is further modified. Moreover, as shown in Figure 2A,B, the Au NCs (circled in yellow dash) are well stabilized and densely anchored onto the LDH nanosheets (marked with red dash) due to the homogeneous distribution of the positive charges within the LDH host layer. The typical top-view scanning electron microscope (SEM) images (Figure S7, Supporting Information) and AFM topographical images (2 µm × 2 µm) of these UTFs (Figure S8 and Table S2, Supporting Information) reveal a homogeneous and uniform surface morphology. The small- angle X-ray diffraction (XRD) pattern (Figure 2C) displays a basal reflection at 2θ = 4.11°, indicating a periodic long-range ordered superlattice structure with a repeated thickness of 2.14 nm. The obtained spacing distance is well consistent with the monolayer arrangement of Au NCs (1.58 nm) in the interlayer region of LDH nanosheets (0.48 nm). The UTF thickness can be estimated based on their side-view SEM images (Figure 2D and Figure S9, Supporting Information), from which an approximately linear increase of film thickness as a function of n is observed with the average thickness increment of 2.30 nm per bilayer cycle (Table S2, Supporting Information). The slight difference between XRD (2.14 nm) and SEM (2.30 nm) may result from the measuring error of different methods, since the d value calculated from the XRD data is a statistical result while the SEM observation is based on every single measurement.

2.3. The Fluorescent Properties of the (Au NCs/LDHs)$_n$ UTFs

The fluorescent properties of Au NCs in aqueous solution and assembled (Au NCs/LDH)$_n$ (n = 0–20) UTFs were also investigated. For Au NCs solution, an emission peak at ≈566 nm (attributed to the triplet transition of the metal-centered nanoclusters) is observed, with a weak orange emission under UV light irradiation (Figure S3, Supporting Information). In contrast, much brighter fluorescence can be observed after the Au NCs localized onto LDH nanosheet for the assembled (Au NCs/LDH)$_n$ (n = 0–20) UTFs with different bilayers (**Figure 3**, inset). The fluorescence spectra of (Au NCs/LDH)$_n$ UTFs (Figure 3) exhibit a gradual increase of emission intensity at ≈560 nm, verifying the incrementally immobilized Au NCs and enhanced fluorescence emission. Moreover, a blue shift (≈6 nm) is observed for the UTFs compared with the pristine solution. The blue shift at ≈560 nm can be related to denser arrangement of adjacent Au(I)-thiol which dominate the emission of Au NCs.[18] This shift is also in accordance with decreased size effect based on the spherical Jellium model.[31]

According to the widely accepted viewpoints, the fluorescence lifetime of NCs could be attributed to ligand-to-metal charge transfer or ligand-to-metal-metal charge transfer and subsequent metal centered triplets, and the microsecond-scale lifetime is dominated by triplet radiation of Au(I)-thiol complexes.[32–36] Herein, the excitation-state lifetime of Au NCs before and after immobilization onto LDH nanosheets was systematically studied and the data were fitted with a double-exponential form. The average fluorescence lifetime for pristine Au NCs is ≈1.84 µs [0.41 µs (38.0%) and 2.72 µs (62.0%), **Figure 4**A and Table S3, Supporting Information], predominated at microsecond scale. After immobilization, the localized Au NCs exhibit superior fluorescent performance, and the lifetime is prolonged to 14.67 µs [5.99 µs (12.26%) and 15.89 µs (87.74%) as shown in Figure 4B and Table S3, Supporting Information]. The largely promoted lifetime of (Au NCs/LDH)$_{20}$ UTF can be attributed to the inhibited nonradiative transition after Au NCs were confined in the interlayer of LDH nanosheets and the corresponding host–guest interaction. Moreover, the QY

© 2015 WILEY-VCH Verlag GmbH & Co. KGaA, Weinheim

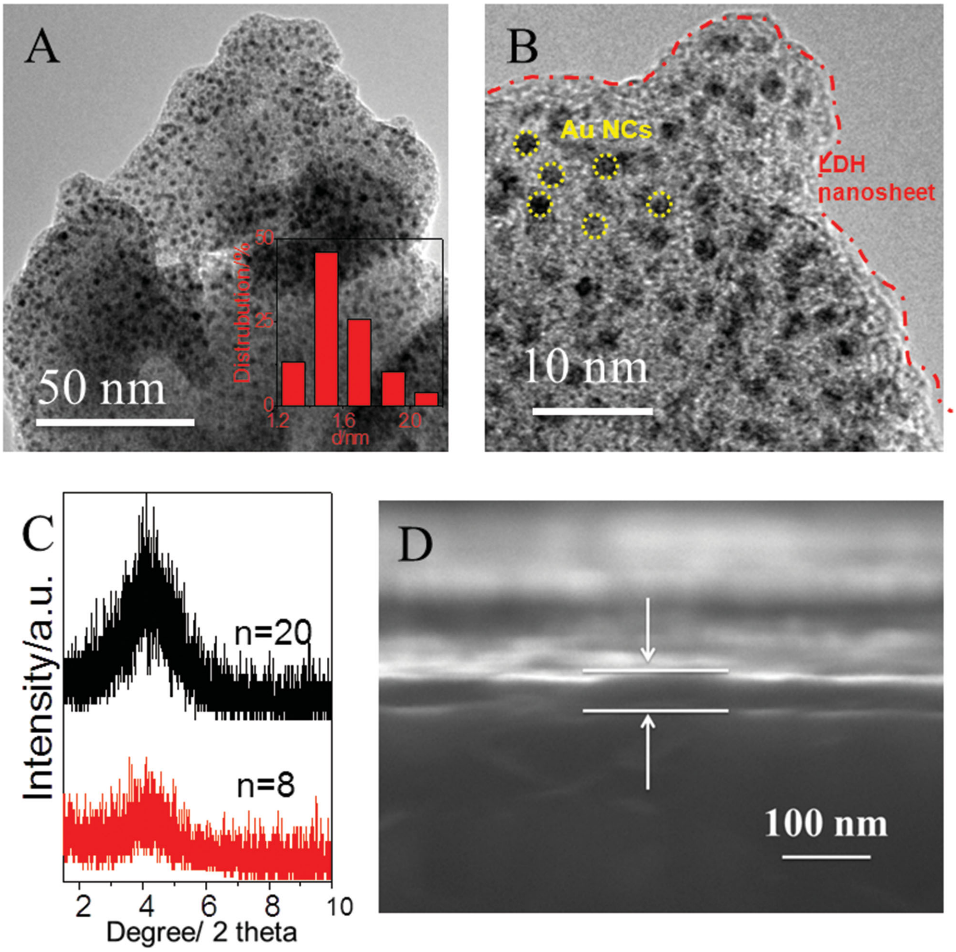

Figure 2. The structural and morphological characterizations of (Au NCs/LDH)$_n$ UTFs: A,B) TEM images with different magnification ($n = 20$); inset in (A) shows the size distribution; red and yellow dashes in (B) are used to mark LDH nanosheet and Au NCs, respectively; C) XRD patterns ($n = 8, 20$) and D) side-view SEM images ($n = 20$).

was also investigated, with a value of 14.11% for the localized Au NCs on LDHs, which is largely improved compared with the value of 2.69% for pristine Au NCs in aqueous. The QY of 14.11% is at a high level compared with film materials based on quantum dots, carbon dots, or upconversion nanoparticles (normally 0.7%–15.7%),[37–39] especially in the orange-red emission region. Moreover, the incorporation of Au NCs into LDH nanosheets improves the QY from aqueous solution to solid films, rather different from the reduction of QY via traditional immobilization methods.[40,41]

2.4. Host–Guest Interactions in the (Au NCs/LDHs)$_n$ UTFs

The influences of host–guest interactions on the improved fluoresent performance were further studied. By adjusting the concentration of Au NCs in aqueous solution for assembly, the loading density of Au NCs can be tuned. The increased concentration of Au NCs from 0.04×10^{-3} to 1.0×10^{-3} M results in a linear enhancement of Au loading density from 1.51 to 60.32 μg cm^{-2} for the (Au NCs/LDH)$_{20}$ UTFs (Figure S11A and Table S4, Supporting Information). This is further observed from TEM images (Figure S10, Supporting Information). The fluorescence emissive position of UTFs with different loading density of Au NCs remains unchanged (at ≈560 nm); and no obvious variation is found for the fluorescence lifetime (ranging in 13.22–14.67 μs; Figure S11D and Table S5, Supporting Information). The results indicate that the interaction between adjacent Au NCs is rather weak and cannot impose distinct influence on the microenvironment of localized Au NCs. In addition, both the PL intensity (Figure S11C, Supporting Information) and brightness (Figure S11B, Supporting Information) increase gradually with the increment of Au NCs density, as a result of the accumulated photoactive species. Another control sample was prepared by mixing LDH nanosheets and Au NCs followed by drop casting on quartz glass substrate. The drop-casted film shows emission at ≈564 nm with a low QY of 6.29%; and nonuniform surface morphology and inhomogeneous fluorescence are observed (Figure S12A and inset, Supporting Information). The superior QY (14.11%) and PL intensity for LbL UTFs (Figure S12C, Supporting Information) compared with the drop-casted film (Figure S12D, Supporting Information) indicate that the confined microenvironment of Au NCs within LDH nanosheets enhances the fluorescence emission.

© 2015 WILEY-VCH Verlag GmbH & Co. KGaA, Weinheim

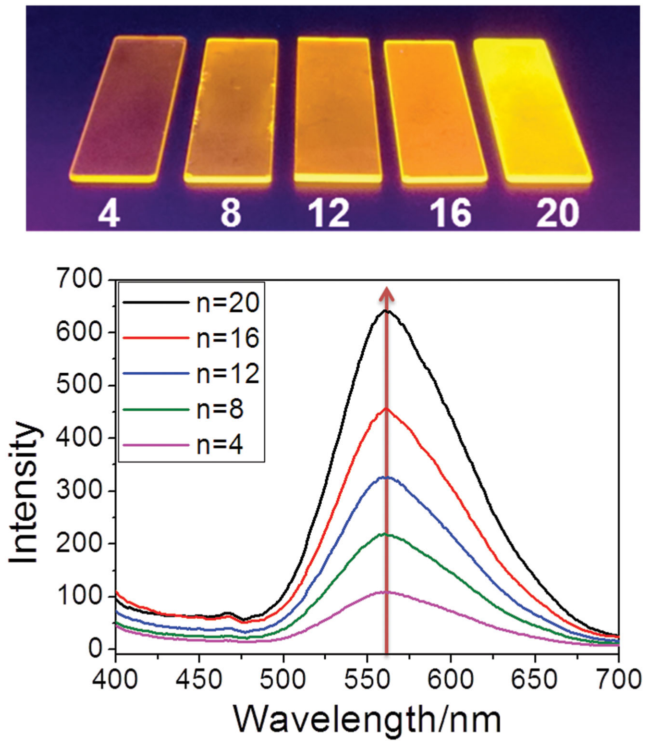

Figure 3. Fluorescence monitoring of (Au NCs/LDH)$_n$ (n = 0–20) UTFs for fluorescence emission spectra; the inset shows the photographs of different bilayers under UV light (exited at 365 nm).

Moreover, XPS was carried out to study the valence state changes of Au NCs before and after immobilization onto LDHs, especially for the emissive Au(I)-thiol portion. **Figure 5**A shows the XPS spectra of drop-casted Au NCs and the oxidation state of Au is located between Au(I)-thiol (pink line, binding energy: 84.7 eV) and Au(0) (green line, binding energy: 83.8 eV). The ratio of the Au(0) to emissive Au(I) state is ≈1.9. Thus, the decisive component of fluorescent emission–Au(I)–was found to constitute 34.4% of all Au atoms in Au NCs. Upon immobilization within LDH nanosheets, the binding energy of Au(I) shifts to 85.4 eV (Figure 5B) and the fraction of Au(I) reaches ≈46.4% with much reduced Au(0)/Au(I) ratio of 1.15. These changes of Au NCs after localization can be attributed to the electrostatic attraction and polarization of interlayer Au NCs induced by positively charged LDH nanosheets. Therefore, the increased active Au(I) content and rearranged charge distribution could optimize the emission state of Au NCs, which could further result in the promoted QY and prolonged lifetime as mentioned above.

To further study the changes of geometric configuration and electronic structure of Au NCs after immobilized on LDH nanosheets, a periodic DFT calculation was employed for the idealized models of pristine Au NCs and Au NCs/LDH structure (**Figure 6**). The optimized geometry of the Au NCs/LDH system is illustrated in Figure 6B with numbers of hydrogen bonds in the interlayer of LDH nanosheets. With the aid of hydrogen bond and electrostatic interactions between Au NCs and LDH nanosheets, the ligands of Au NCs are rearranged with most COO^- groups in glutathione ligands (SG) attaching to LDH nanosheets, while the ligands of pristine Au NCs is expanded to form a pseudo-spherical structure (Figure 6A). The changed configuration leads to a reduced particle size of Au NC (1.51 nm) in the LDH nanogallery, in agreement with the experimental XRD (1.66 nm) and TEM (1.58 nm) results. DFT calculations reveal that the Au NCs is tightly localized and confined in the microenvironment via the host–guest hydrogen bond and electrostatic interactions, resulting in the enhanced fluorescence emission as observed by experimental studies. The vibration and rotation of Au NCs are inhibited to a great extent and the corresponding nonradiation process is reduced, which results in promoted fluorescent performance as in experiment. Moreover, top view of the optimized geometry (Figure S13, Supporting Information) illustrates that the nearest distance between adjacent Au NCs is 5.6 Å, which exceeds the distance region of aurophilic interaction (3.3 Å) reported previously.[42,43] Based on our experimental results and previous work, it is proposed that the distance between adjacent Au NCs in this work is large enough to ignore their interactions.

In addition, the charge variation of Au atoms was studied so as to understand the charge transfer of NCs after localized on LDH nanosheets. It is found that the total Hirshfeld charge of Au atoms in the single NC increases from 0.770 e to 1.433 e upon interaction with LDH layers (Table S6, Supporting Information), indicating that electron transfer occurs from Au NCs to LDH nanosheets due to the electrostatic interactions and polarization effect of LDH layers. Therefore, more positively charged Au(I) can be obtained for the Au NCs, which is

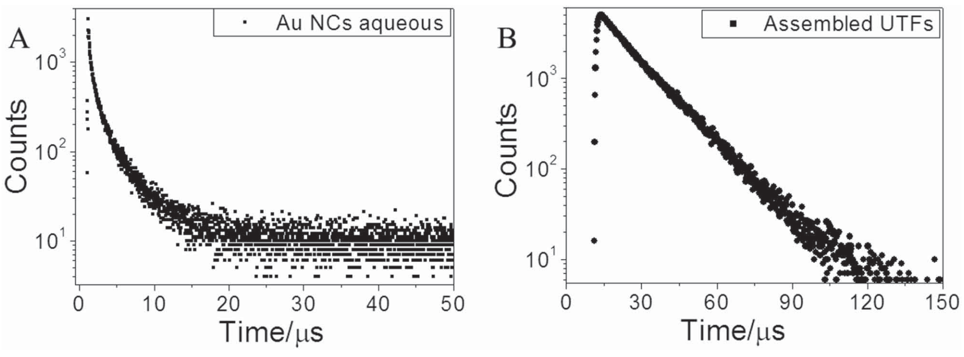

Figure 4. Typical fluorescence decay curves of A) Au NCs in aqueous solution and B) the (Au NCs/LDH)$_{20}$ UTF.

© 2015 WILEY-VCH Verlag GmbH & Co. KGaA, Weinheim

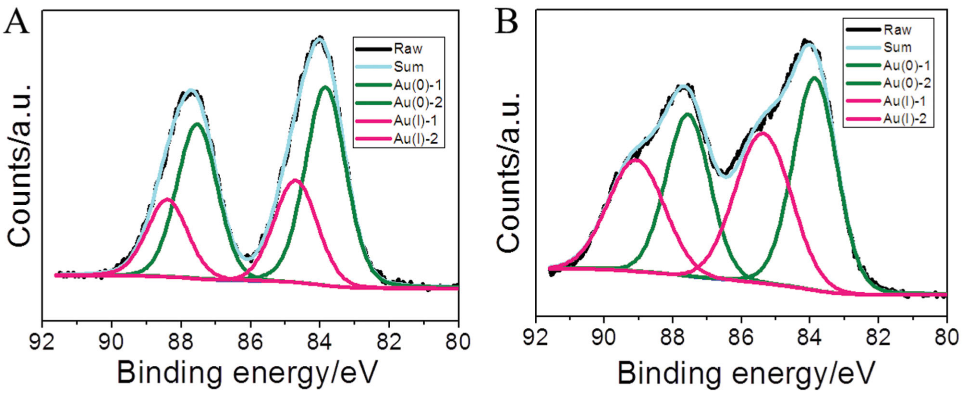

Figure 5. XPS analysis of A) pristine Au NCs and B) assembled (Au NCs/LDH)$_{20}$ UTF.

consistent with the XPS results of increased Au(I) content. It thus can be concluded that Au NCs undergo changes in geometric configuration and charge distribution within the 2D gallery of LDH nanosheets, which accounts for the confinement-induced emission enhancement.

2.5. The Temperature-Responsive Luminescence of the (Au NCs/LDHs)$_n$ UTFs

To develop potential luminescent sensor application for the immobilized (Au NCs/LDHs)$_n$ UTFs, temperature-dependent PL and ECL were performed. For the (Au NCs/LDHs)$_{20}$ UTF, a visible luminescence intensity change is observed by the naked eye in the temperature range 20–90 °C (**Figure** 7B). Upon heating, the luminescence intensity of the (Au NCs/LDHs)$_{20}$ UTF displays a gradual decrease, with a linear response sensitivity about –1.05% °C^{-1} (Figure 7A); while no linear correlation can be found for the pristine Au NCs in aqueous solution versus temperature (Figure S14, Supporting Information). This phenomenon can be attributed to the well-organized thermal motion of localized Au NCs on LDH nanosheets in contrast to the disordered state in aqueous solution. When the UTF is cooled to 20 °C, it can recover its original luminescent intensity completely. The reversible measurements show the readily repeated luminescent intensity changes for at least eight cycles (Figure 7C). Moreover, fluorescence lifetimes at 20 °C and 80 °C were measured to further study the excited states of UTF. As shown in Figure 7D, the fluorescence decay at 20 °C (12.50 µs) is slower compared with that at 80 °C (10.11 µs, Table S7, Supporting Information). The decreased lifetime indicates enhanced nonradiative processes related to thermal agitation at high temperature, in accordance with the reduced luminescent intensity. It is found that the (Au NCs/LDH)$_{20}$ UTF is rather stable in water. No obvious change is observed for the film after the temperature-dependent PL measurements in water (Figure S15A, Supporting Information) and no distinct species leaching into water occurs (Figure S15B, Supporting Information).

ECL is another important approach to produce luminescence during electrochemical reactions in solutions. Herein, to extend the Au NCs as an ECL detection device, the ECL performances of the (Au NCs/LDHs)$_{20}$ UTF on ITO (indium tin oxide) glass were studied in 0.1 M phosphate buffer saline containing 0.1 M KCl as electrolyte and 0.1 M $K_2S_2O_8$ as coreactants. The cyclic voltammetry (CV) curve and ECL signal were obtained between +2.0 and –1.5 V at a scan rate of 0.1 V s^{-1}. As shown in **Figure** 8A,B, an obvious ECL signal is observed

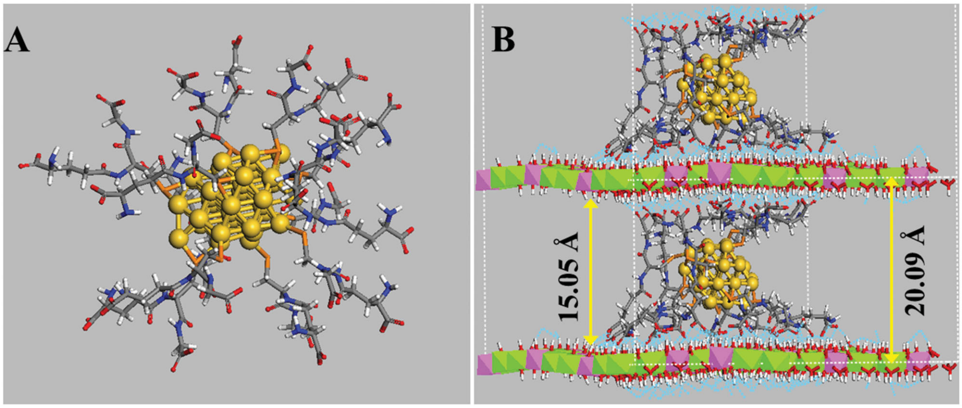

Figure 6. Optimized geometry of A) pristine Au NCs [$Au_{36}(SG)_{12}$] and B) assembled Au NC/LDH structure model (color denotation: green for Mg, pink for Al, red for O, golden for Au, white for H, grey for C, blue for N, and orange for S). The hydrogen bond is displayed by blue dashed lines.

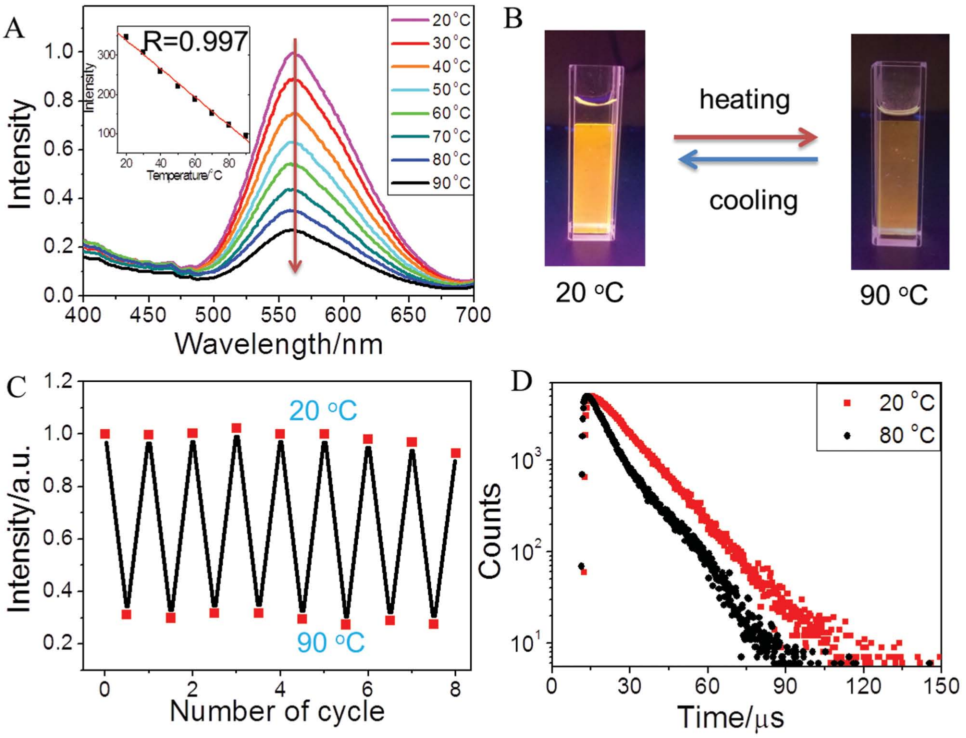

Figure 7. Photoluminescence responses toward temperature for the (Au NCs/LDH)$_{20}$ UTF in the range 20–90 °C stabilized in water: A) fluorescence emission spectra (the inset shows the changes of intensity at ≈560 nm), B) photographs taken under UV light (365 nm), C) reversibility test, and D) typical fluorescence decay curves of (Au NCs/LDH)$_{20}$ UTF at 20 °C (red) and 80 °C (black).

for the (Au NCs/LDHs)$_{20}$ UTF with light emission at ≈–1.3 V and the intense signal remains rather stable for six cycles. The possible ECL mechanisms can be deduced as the following equation:[44]

$$(\mathrm{Au/LDH}) + e^- \rightarrow (\mathrm{Au/LDH})^{\bullet -} \quad (1)$$

$$\mathrm{S_2O_8^{2-}} + e^- \rightarrow \mathrm{SO_4^{2-}} + \mathrm{SO_4^{\bullet -}} \quad (2)$$

$$(\mathrm{Au/LDH})^{\bullet -} + \mathrm{SO_4^{\bullet -}} \rightarrow (\mathrm{Au/LDH})^* + \mathrm{SO_4^{2-}} \quad (3)$$

$$(\mathrm{Au/LDH})^* \rightarrow (\mathrm{Au/LDH}) + h\nu \quad (4)$$

Compared with bare ITO (black line in Figure 8A), the (Au NCs/LDHs)$_{20}$/ITO (red line in Figure 8A) exhibits one broad oxidation peak in the potential range 1.35–1.62 V, which corresponds to the reaction from (Au/LDH)$^{\bullet -}$ to (Au/LDH)*.[45] As the density of localized Au NCs increases, ECL signals are promoted accordingly (Figure S16, Supporting Information). As reference samples, the ECL performance of pristine Au NCs in aqueous solution and drop-casted film were also measured. Au NCs in aqueous solution exhibit no obvious signal (Figure S17, Supporting Information); and the Au NCs drop-casted film shows continuously decreased signal intensity (Figure S18, Supporting Information). Moreover, ECL performances of (Au NCs/LDH)$_{20}$ UTF at different temperatures (20, 50, and 80 °C) were studied, which showed that the ECL intensity of (Au NCs/LDH)$_{20}$ UTF decreases gradually along with elevated temperature (Figure 8C); additionally, a stable signal intensity at each temperature level is observed. To the best of our knowledge, temperature-dependent ECL phenomenon based on metal NCs systems has been barely reported previously, and thus the Au NCs-based film material may supply an effective platform to develop potential temperature-responsive ECL device.

2.6. Stability of (Au NCs/LDHs)$_n$ UTFs

To develop potential Au NCs-based luminescence sensor devices, stability is a crucial factor, and thus a long-term stability of the (Au NCs/LDH)$_{20}$ UTF was also studied upon irradiation under UV light for 2 h in comparison with drop-casted Au NCs films (**Figure 9**A). After a 2 h irradiation, the PL intensity at ≈560 nm decreases to 75% of its original value for the Au NCs casted film; while the (Au NCs/LDH)$_{20}$ UTF only exhibits a 10% decrease under the same conditions. The less stability of bare Au NCs-containing film is possibly due to the disruption of Au–S bond under UV light, while the employment of LDH nanosheets could provide a strong protection for Au–S bonding due to the absorbance and scattering of UV light as well as host–guest interactions.[46] The nanogallery microenvironment could avoid aggregation of the NCs into large nanoparticles and further enable excellent photostability of the Au NCs with negligible photobleaching during the irradiation period. In addition, photoluminescence blinking is a universal property of molecular emitters found in various fluophores (such as organic dyes and quantum

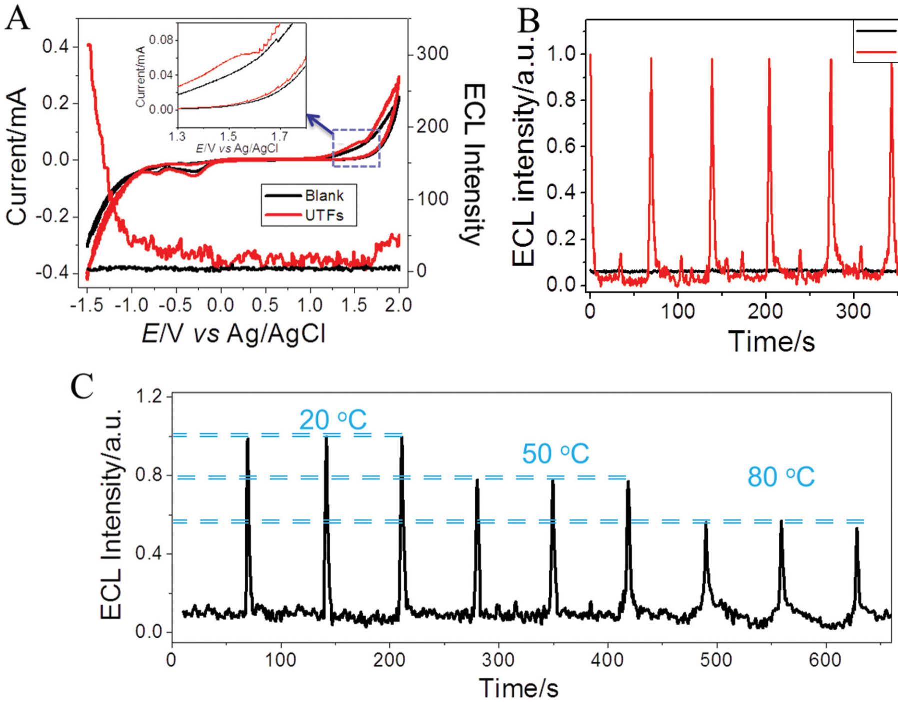

Figure 8. A) CV curves and B) ECL signal of bare ITO glass (black) and the (Au NCs/LDH)$_{20}$ UTF (red), and C) temperature-dependent response of ECL signal for the (Au NCs/LDH)$_{20}$ UTF.

dots) which severely limited their application in display and cell tracking.[47,48] Therefore, PL blinking test was also carried out for (Au NCs/LDH)$_{20}$ UTFs in a period of 16 s with the excitation interval of 10 ms. Intensity time-traces recorded in Figure 9B show that no fluorescence intermittency occurs for Au NCs, which is a superior property compared with the traditional dyes and quantum dots.[49–52] The inset in Figure 9B confirms the continuous fluorescence emission along with time, as a result of the depressed motion or frequency shift of Au NCs within the gallery of LDH nanosheets. Therefore, the assembled (Au NCs/LDH)$_{20}$ UTF exhibits advanced stability and nonblinking property, which are beneficial to their future applications in photonic/optoelectronic devices and bioimaging.[53,54]

3. Conclusions

In this work, Au NCs-based UTFs with high QY and long lifetime have been achieved through a layer-by-layer assembly with LDH nanosheets. The as-fabricated (Au NCs/LDH)$_n$ UTFs exhibit an ordered structure with Au NCs anchoring onto LDH nanosheets densely and uniformly. Due to the host–guest interaction (e.g., electrostatic force and hydrogen bonding), Au NCs are stabilized in the confined environment of LDH nanosheets, resulting in reduced nonradiative transition and thus enhanced fluorescent performances. The electropositivity of LDH nanosheets impose significant influences on the configuration and valence state of Au NCs with the content of Au(I)-thiol promoted to 46.4%, accounting for the high QY

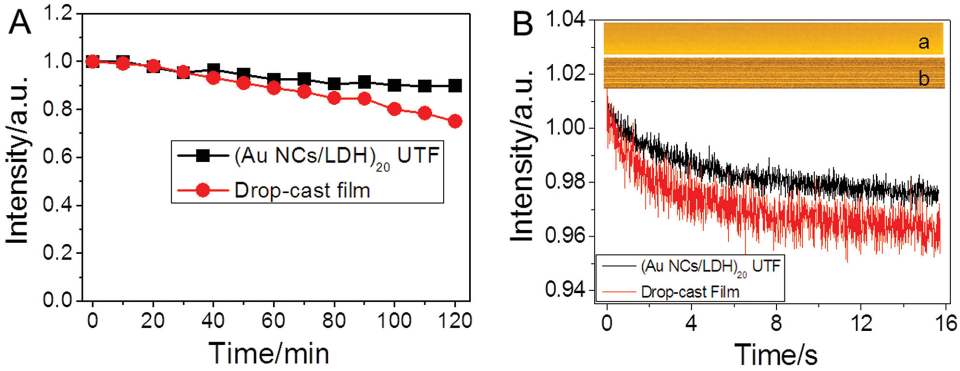

Figure 9. A) Photostability and B) fluorescence intensity traces of the (Au NCs/LDH)$_{20}$ UTF (black) and drop-casted Au NCs on glass (red) versus laser irradiation time; inset in (B) shows the fluorescence emission changes along with time for a) (Au NCs/LDH)$_{20}$ UTF and b) drop-cast film.

© 2015 WILEY-VCH Verlag GmbH & Co. KGaA, Weinheim

and long lifetime as confirmed by both experimental and computational studies. Moreover, the UTFs exhibit temperature-dependent response both in PL and ECL measurements, and the good stability and nonblinking properties further guarantee its practical application. Therefore, the strategy based on the localization and confinement of Au NCs onto LDH nanosheets achieves largely enhanced fluorescent properties of Au NCs, which would enable their potential applications in temperature-responsive devices. It is also expected that such strategy can be extended to other metal NCs systems with unique luminescent performances.

4. Experimental Section

Materials: L-Glutathione in the reduced form (GSH) was obtained from Sigma-Aldrich. Hydrogen tetrachloroaurate hydrate ($HAuCl_4•3H_2O$, >99.9%), analytical-grade chemicals including formamide, $Mg(NO_3)_2·6H_2O$, $Al(NO_3)_3·9H_2O$, and HNO_3 were purchased from Aladdin Chemical. Co. Ltd. Ultrapure water from a Milli-Q Millipore system was used as the general solvent in all the experimental processes.

Preparation of Au NCs: The aqueous synthesis of Au NCs reduced by GSH was referred to the as-reported method.[18] In a typical synthesis, 1.0 mL of $HAuCl_4·3H_2O$ (20×10^{-3} M) was mixed with 0.30 mL of GSH (100×10^{-3} M), followed by adding 8.7 mL of ultrapure water at 25 °C. The solution was heated to 70 °C under stirring for 24 h and the obtained Au NCs in aqueous solution was cooled to room temperature and stored at 4 °C.

Fabrication of (Au NCs/LDH)$_n$ UTFs: The preparation of MgAl-LDH nanosheets was similar with our previous work.[55,56] Formamide (100 mL) was used in exfoliation of the as-prepared nitrate MgAl-LDH (0.1 g) to obtain a colloidal suspension of MgAl-LDH nanosheets. The prepared Au NCs in aqueous solution has been diluted to 1×10^{-3}, 0.4×10^{-3}, 0.2×10^{-3}, 0.1×10^{-3}, and 0.04×10^{-3} M for LbL assembly. The substrate of quartz glass was treated by the mixed H_2SO_4.30% H_2O_2 (7:3, v/v) solution for 30 min, followed by another 30 min in ethanol to remove the possible organics. In order to fabricate the (Au NCs/LDH)$_n$ films, the negatively charged substrate was firstly dipped into LDH nanosheets (1 g L^{-1}) for 10 min followed by washing thoroughly, and then immersed into the Au NCs solution for another 10 min. Fabrication of multilayered (Au NCs/LDH)$_n$ UTFs was performed by the repeat alternation in LDH nanosheets and Au NCs aqueous solution for *n* cycles, followed by thoroughly washing and drying.

Sample Characterization: TEM images were recorded on a JEOL JEM-2100 TEM with the accelerating voltage of 200 kV. The UV–vis absorption spectra were collected in the range from 300 to 800 nm on a Shimadzu U-3000 spectrophotometer, with the slit width of 1.0 nm. The fluorescence spectra were performed on a RF-5301PC fluorospectrophotometer with the excitation wavelength of 360 nm. The fluorescence emission spectra range in 400–700 nm, and both the excitation and emission slit are set to be 5 nm. XRD patterns of the UTFs were recorded using a Rigaku 2500 VB2 + PC diffractometer under the conditions: 40 kV, 50 mA, Cu K radiation ($\lambda = 0.1541$ nm) with step scanned in step of 0.04 (2θ) in the range from 1° to 10° using a count time of 10 s step^{-1}. The morphology of thin films was investigated by using a scanning electron microscope (Hitachi S-3500) and the accelerating voltage applied was 20 kV. The surface roughness data were obtained by using the NanoScope IIIa AFM from Veeco Instruments. XPS measurements were performed using an ESCALAB 250 instrument (Thermo Electron) with Al Ka radiation. Steady-state luminescence lifetime measurements were recorded with an Edinburgh FLS 980 Lifetime and Steady State Spectrometer. Photoluminescence quantum yield was measured using the reconvolution fit analysis (Edinburgh F980 analysis software) equipped with an integrating sphere. The blinking tests were performed on a zeiss 510META confocal microscope.

PL and ECL Responses Toward Temperature: PL responses toward temperature were carried out by dipping the (Au NCs/LDH)$_{20}$ UTFs into water at different temperature to ensure the accurate temperature of UTFs. ECL measurements were performed using a conventional three-electrode system, involving platinum foil and saturated Ag/AgCl electrode (0.799 V) as the auxiliary and reference electrode, respectively. (Au NCs/LDH)$_n$ UTF was assembled on ITO glass as the working electrode. The ECL signals were recorded by a MPI-B multifunctional chemiluminescent analytical system (Remax Electronic Co. Ltd., Xi'an, China) by setting the voltage of the photomultiplier tube at 800 V. Temperature-dependent ECL signals were measured at 20, 50, and 80 °C, respectively. The content of samples was determined by ICP-AES on a Shimadzu ICPS-7500 instrument.

Structural Model of Au NCs and Au NCs/LDH System: The model of MgAl-LDHs was built based on the structure of brucite.[57] The supercell model with molar ratio Mg/Al = 2 was $8 \times 9 \times 1$ in the *a*-, *b*-, and *c*-direction, respectively, containing 48 Mg^{2+}, 24 Al^{3+}, and 144 OH groups in each octahedral layer. The model of Au NCs was built by creating an SG shell around the Au NPs precursor units. SG molecules and Au atoms are connected by S–Au bond. Since exact experimental data for the amount of SG ligands attaching to each Au core are not available, the number of SG units was estimated by considering the charge density of LDHs interlayer spacing, which possesses a charge of 24 e in the interlayer gallery with a volume of $\approx 1.2 \times 10^4$ Å^3. Therefore, 12 SG ligands were employed to simulate the interaction between SG molecules and Au core containing 36 Au atoms.[58–60]

Periodic Density Functional Theory (DFT) Calculation: DFT method was performed using Dmol3 code in the Materials Studio 5.5 software package.[61–63] The exchange-correlation potential was calculated by the Perdew–Burke–Ernzerhof (PBE) generalized gradient approach.[64–67] A double number basis sets plus polarization function were used to describe the atomic orbitals. Effective core potentials were employed to treat the core electrons for Au atoms. An energy tolerance of 5.40×10^{-4} eV per atom with a maximum tolerance of 0.11 eV Å^{-1} was adopted as the convergence criteria. The *k*-space is sampled by the γ point.

Supporting Information

Supporting Information is available from the Wiley Online Library or from the author.

Acknowledgements

This work was supported by the 973 Program (Grant No. 2014CB932104), the National Natural Science Foundation of China (NSFC), the Beijing Natural Science Foundation (2132043), and the Specialized Research Fund for the Doctoral Program of Higher Education (20130010110013). M.W. particularly appreciates the financial aid from the China National Funds for Distinguished Young Scientists of the NSFC.

Received: April 9, 2015
Revised: May 22, 2015
Published online: July 8, 2015

---

[1] M. A. H. Muhammed, P. K. Verma, S. K. Pal, A. Retnakumari, M. Koyakutty, S. Nair, T. Pradeep, *Chem. Eur. J.* **2010**, *16*, 10103.
[2] S. H. Yau, O. Varnavski, T. Goodson, *Acc. Chem. Res.* **2013**, *46*, 1506.
[3] Z. Wu, J. Chen, R. Jin, *Adv. Funct. Mater.* **2011**, *21*, 177.
[4] Z. Luo, K. Zheng, J. Xie, *Chem. Commun.* **2014**, *50*, 5143.
[5] J. Liu, *TrAC Trend Anal. Chem.* **2014**, *58*, 99.
[6] D. Chen, Z. Luo, N. Li, J. Y. Lee, J. Xie, J. Lu, *Adv. Funct. Mater.* **2013**, *23*, 4324.
[7] Y. Tao, E. Ju, Z. Li, J. Ren, X. Qu, *Adv. Funct. Mater.* **2014**, *24*, 1004.
[8] J. Xie, Y. Zheng, J. Y. Ying, *J. Am. Chem. Soc.* **2009**, *131*, 888.

[9] L. Li, L. Dou, H. Zhang, *Nanoscale* **2014**, *6*, 3753.
[10] S. Roy, A. Baral, A. Banerjee, *ACS Appl. Mater. Interfaces* **2014**, *6*, 4050.
[11] H. Kawasaki, K. Hamaguchi, I. Osaka, R. Arakawa, *Adv. Funct. Mater.* **2011**, *21*, 3508.
[12] Y. Liu, K. Ai, X. Cheng, L. Huo, L. Lu, *Adv. Funct. Mater.* **2010**, *20*, 951.
[13] M. A. H. Muhammed, P. K. Verma, S. K. Pal, R. C. A. Kumar, S. Paul, R. V. Omkumar, T. Pradeep, *Chem. Eur. J.* **2009**, *15*, 10110.
[14] X. Le Guével, V. Trouillet, C. Spies, K. Li, T. Laaksonen, D. Auerbach, G. Jung, M. Schneider, *Nanoscale* **2012**, *4*, 7624.
[15] Y. Chen, T. Yang, H. Pan, Y. Yuan, L. Chen, M. Liu, K. Zhang, S. Zhang, P. Wu, J. Xu, *J. Am. Chem. Soc.* **2014**, *136*, 1686.
[16] S. Link, A. Beeby, S. FitzGerald, M. A. El-Sayed, T. G. Schaaff, R. L. Whetten, *J. Phys. Chem. B* **2002**, *106*, 3410.
[17] H.-W. Li, Y. Yue, T.-Y. Liu, D. Li, Y. Wu, *J. Phys. Chem. C* **2013**, *117*, 16159.
[18] Z. Luo, X. Yuan, Y. Yu, Q. Zhang, D. T. Leong, J. Y. Lee, J. Xie, *J. Am. Chem. Soc.* **2012**, *134*, 16662.
[19] X. Yuan, Z. Luo, Y. Yu, Q. Yao, J. Xie, *Chem. Asian J.* **2013**, *8*, 858.
[20] L. Shang, S. Brandholt, F. Stockmar, V. Trouillet, M. Bruns, G. U. Nienhaus, *Small* **2012**, *8*, 661.
[21] G. De Cremer, Y. Antoku, M. B. J. Roeffaers, M. Sliwa, J. Van Noyen, S. Smout, J. Hofkens, D. E. De Vos, B. F. Sels, T. Vosch, *Angew. Chem. Int. Ed.* **2008**, *47*, 2813.
[22] M. Bellec, A. Royon, K. Bourhis, J. Choi, B. Bousquet, M. Treguer, T. Cardinal, J.-J. Videau, M. Richardson, L. Canioni, *J. Phys. Chem. C* **2010**, *114*, 15584.
[23] J. A. Gursky, S. D. Blough, C. Luna, C. Gomez, A. N. Luevano, E. A. Gardner, *J. Am. Chem. Soc.* **2006**, *128*, 8376.
[24] D. Yan, J. Lu, M. Wei, D. G. Evans, X. Duan, *J. Mater. Chem.* **2011**, *21*, 13128.
[25] A. M. Fogg, V. M. Green, H. G. Harvey, D. O'Hare, *Adv. Mater.* **1999**, *11*, 1466.
[26] D. Yan, A. Delori, G. O. Lloyd, B. Patel, T. Friščić, G. M. Day, D.-K. Bučar, W. Jones, J. Lu, M. Wei, D. G. Evans, X. Duan, *CrystEngComm* **2012**, *14*, 5121.
[27] M.-Q. Zhao, Q. Zhang, J.-Q. Huang, F. Wei, *Adv. Funct. Mater.* **2012**, *22*, 675.
[28] L. Shang, S. Dong, G. U. Nienhaus, *Nano Today* **2011**, *6*, 401.
[29] L. Li, R. Ma, Y. Ebina, N. Iyi, T. Sasaki, *Chem. Mater.* **2005**, *17*, 4386.
[30] J. Han, X. Xu, X. Rao, M. Wei, D. G. Evans, X. Duan, *J. Mater. Chem.* **2011**, *21*, 2126.
[31] J. Zheng, C. Zhang, R. Dickson, *Phys. Rev. Lett.* **2004**, *93*, 077402-1.
[32] S.-H. Cha, J.-U. Kim, K.-H. Kim, J.-C. Lee, *Chem. Mater.* **2007**, *19*, 6297.
[33] C.-K. Li, X.-X. Lu, K. M.-C. Wong, C.-L. Chan, N. Zhu, V. W.-W. Yam, *Inorg. Chem.* **2004**, *43*, 7421.
[34] Y. Yang, Q. Zhao, W. Feng, F. Li, *Chem. Rev.* **2013**, *113*, 192.
[35] J. M. Forward, D. Bohmann, J. P. FacklerJr, R. J. Staples, *Inorg. Chem.* **1995**, *34*, 6330.
[36] V. W.-W. Yam, C.-K. Li, C.-L. Chan, *Angew. Chem. Int. Ed.* **1998**, *37*, 2857.
[37] C. C. Shih, P. C. Chen, G. L. Lin, C. W. Wang, H. T. Chang, *ACS Nano* **2015**, *9*, 312.
[38] R. Liang, S. Xu, D. Yan, W. Shi, R. Tian, H. Yan, M. Wei, D. G. Evans, X. Duan, *Adv. Funct. Mater.* **2012**, *22*, 4940.
[39] M. Saboktakin, X. Ye, S. J. Oh, S. H. Hong, A. T. Fafarman, U. K. Chettiar, N. Engheta, C. B. Murray, C. R. Kagan, *ACS Nano* **2012**, *6*, 8758.
[40] D. Pan, J. Zhang, Z. Li, Z. Zhang, L. Guo, M. Wu, *J. Mater. Chem.* **2011**, *21*, 3565.
[41] Y. W. Lin, W. L. Tseng, H. T. Chang, *Adv. Mater.* **2006**, *18*, 1381.
[42] S.-H. Cha, J.-U. Kim, K.-H. Kim, J.-C. Lee, *Chem. Mater.* **2007**, *19*, 6297.
[43] H. Ito, T. Saito, N. Oshima, N. Kitamura, S. Ishizaka, Y. Hinatsu, M. Wakeshima, M. Kato, K. Tsuge, M. Sawamura, *J. Am. Chem. Soc.* **2008**, *130*, 10044.
[44] W. Guo, J. Yuan, E. Wang, *Chem. Commun.* **2012**, *48*, 3076.
[45] L. Li, H. Liu, Y. Shen, J. Zhang, J.-J. Zhu, *Anal. Chem.* **2011**, *83*, 661.
[46] W. Shi, Y. Lin, S. Zhang, R. Tian, R. Liang, M. Wei, D. G. Evans, X. Duan, *Phys. Chem. Chem. Phys.* **2013**, *15*, 18217.
[47] C. Galland, Y. Ghosh, A. Steinbrück, M. Sykora, J. A. Hollingsworth, V. I. Klimov, H. Htoon, *Nature* **2011**, *479*, 203.
[48] X. Wang, X. Ren, K. Kahen, M. A. Hahn, M. Rajeswaran, S. Maccagnano-Zacher, J. Silcox, G. E. Cragg, A. L. Efros, T. D. Krauss, *Nature* **2009**, *459*, 686.
[49] B. Mahler, P. Spinicelli, S. Buil, X. Quelin, J.-P. Hermier, B. Dubertret, *Nat. Mater.* **2008**, *7*, 659.
[50] Z. Xu, M. Cotlet, *Small* **2012**, *8*, 253.
[51] L. Polavarapu, M. Manna, Q.-H. Xu, *Nanoscale* **2011**, *3*, 429.
[52] T. Vosch, Y. Antoku, J. C. Hsiang, C. I. Richards, J. I. Gonzalez, R. M. Dickson, *Proc. Natl. Acad. Sci. USA* **2007**, *104*, 12616.
[53] C. Galland, Y. Ghosh, A. Steinbrück, M. Sykora, J. A. Hollingsworth, V. I. Klimov, H. Htoon, *Nature* **2011**, *479*, 203.
[54] X. Wang, X. Ren, K. Kahen, M. A. Hahn, M. Rajeswaran, S. Maccagnano-Zacher, J. Silcox, G. E. Cragg, A. L. Efros, T. D. Krauss, *Nature* **2009**, *459*, 686.
[55] D. Yan, J. Lu, M. Wei, S. Qin, L. Chen, S. Zhang, D. G. Evans, X. Duan, *Adv. Funct. Mater.* **2011**, *21*, 2497.
[56] R. Tian, R. Liang, D. Yan, W. Shi, X. Yu, M. Wei, L. S. Li, D. G. Evans, X. Duan, *J. Mater. Chem. C* **2013**, *1*, 5654.
[57] G. Isetti, *Period. Mineral.* **1965**, *34*, 327.
[58] S. Roy, A. Baral, R. Bhattacharjee, B. Jana, A. Datta, S. Ghosh, A. Banerjee, *Nanoscale* **2015**, *7*, 1912.
[59] F. Behafarid, J. Matos, S. Hong, L. Zhang, T. S. Rahman, B. R. Cuenya, *ACS Nano* **2014**, *8*, 6671.
[60] C. Zeng, H. Qian, T. Li, G. Li, N. L. Rosi, B. Yoon, R. N. Barnett, R. L. Whetten, U. Landman, R. Jin, *Angew. Chem. Int. Ed.* **2012**, *51*, 13114.
[61] B. Delley, *J. Chem. Phys.* **1990**, *92*, 508.
[62] B. Delley, *J. Chem. Phys.* **1996**, *100*, 6107.
[63] B. Delley, *J. Chem. Phys.* **2000**, *113*, 7756.
[64] J. P. Perdew, J. A. Chevary, S. H. Vosko, K. A. Jackson, M. R. Perderson, D. J. Singh, C. Fiolhais, *Phys. Rev. B* **1992**, *46*, 6671.
[65] J. P. Perdew, J. A. Chevary, S. H. Vosko, K. A. Jackson, M. R. Perderson, D. J. Singh, C. Fiolhais, *Phys. Rev. B* **1993**, *48*, 4978.
[66] J. P. Perdew, K. Burke, Y. Wang, *Phys. Rev. B* **1996**, *54*, 16533.
[67] J. P. Perdew, K. Burke, Y. Wang, *Phys. Rev. B* **1998**, *57*, 14999.

© 2015 WILEY-VCH Verlag GmbH & Co. KGaA, Weinheim